# FeP: Another Attractive Anode for the Li-Ion Battery Enlisting a Reversible Two-Step Insertion/Conversion Process

S. Boyanov,[†] J. Bernardi,[‡] F. Gillot,[§] L. Dupont,[§] M. Womes,[†] J.-M. Tarascon,[§] L. Monconduit,[†] and M.-L. Doublet*[,‡]

*LAMMI-CNRS 5072 and LSDSMS-CNRS 5636, Université Montpellier II, Place E. Bataillon, F34095 Montpellier, France, and LRCS-CNRS 6007, Université de Picardie Jules Verne, 33, rue Saint-Leu, F80039 Amiens, France*

*Received February 21, 2006. Revised Manuscript Received April 27, 2006*

$FeP_y$ ($y = 1, 2, 4$) anodes all react with lithium through a conversion reaction $FeP_y + 3yLi \rightarrow yLi_3P + Fe^0$ in their first discharge, leading to nanocomposite discharged electrodes described by nanosized $Fe^0$ particles embedded in $yLi_3P$ matrixes. From electrochemical and complementary in situ X-ray diffraction and high-resolution transmission electron microscopy studies, we deduce that the conversion reaction occurring during the first discharge is followed by two successive insertion and conversion processes in further cycles for the FeP electrode. The insertion process is highly reversible, leading to a capacity retention of 300 mA h $g^{-1}$ and 1900 mA h $cm^{-3}$ after 100 cycles, and corresponds to the formation of an intermediate tetragonal LiFeP phase as deduced from first-principles $T = 0$ K phase diagram calculations and preliminary Mössbauer analyses. We expect the kinetics of this reaction to be strongly limited by the increase in $y$, thus leading to an increasing capacity fading when increasing the $y$ P/Fe ratio.

## 1. Introduction

Recent efforts toward the design of new negative electrode materials for Li-ion batteries have led to binary[1−6] and ternary transition metal phosphides[7−10] exhibiting high gravimetric and volumetric capacities associated with small electrode volume expansions. The numerous transition metal phosphides reported so far display different redox reactions depending on the 3d transition metal. With early transition metals (M = Ti, V), lithium insertion in either the binary $MP_y$ or the ternary $Li_xMP_y$ electrodes proceeds through classical insertion mechanisms,[7−9,11] while with middle and late transition metals (M = Mn, Fe, Co, Ni), it generally proceeds through the conversion of $MP_y$ into a composite electrode made of metallic nanosized particles embedded in a $Li_3P$ matrix through the reaction $MP_y + 3yLi \rightarrow yLi_3P + M^0$.[1,2,5] These so-called conversion reactions, which have already been demonstrated for oxides,[12] sulfides,[13] and fluorides,[14] provide a breakthrough in the search for increasing electrode capacities, because they offer a new type of energy storage involving the exchange of 3$y$Li per transition metal. However, they give rise to several fundamental questions regarding both their driving force and their reversibility, as depicted by the different studies reported so far. From a general point of view, all $MP_y$ systems for which a conversion reaction was clearly demonstrated in the first discharge show a significant capacity loss on further charge. This obviously questions the $MP_y$ reconstruction in oxidation and, therefore, raises the question of the redox center involved after the first discharge conversion reaction. Starting with the $CoP_3$ electrode, Nazar et al. have shown that the $Li_3P$ phase formed after the conversion of $CoP_3$ becomes the redox center on further cycles, leading to a reversible reaction $Li_3P \leftrightarrow LiP + 2Li$.[2] For $FeP_2$, the same authors have suggested an insertion mechanism instead of a conversion reaction on discharge, leading to the formation of a metastable and nanostructured $Fe_xP-Li_yP-Fe_x$ electrode.[4] For both $MnP_4$ and the monoclinic form of $NiP_2$, we have demonstrated a two-step insertion/conversion during the first discharge, leading to the formation of intermediate ternary $Li_xMP_y$ phases[5,6] and preceding the $Li_xMP_y + (3y - x)Li \rightarrow$

* Corresponding author. E-mail: doublet@univ-montp2.fr.
† LAMMI-CNRS 5072, Université Montpellier II.
‡ LSDSMS-CNRS 5636, Université Montpellier II.
§ Université de Picardie Jules Verne.

(1) Alcantara, R.; Tirado, J. L.; Jumas, J. C.; Monconduit, L.; Fourcade, J. O. *J. Power Sources* **2002**, *109*, 308.
(2) Pralong, V.; Souza, D. C. S.; Leunge, K. T.; Nazar, L. F. *Electrochem. Commun.* **2002**, *4*, 516.
(3) Souza, D. C. S.; Pralong, V.; Jacobson, A. J.; Nazar, L. F. *Science* **2002**, *296*, 2012.
(4) Silva, D. C. C.; Crosnier, O.; Ouvrard, G.; Greedan, J.; Safa-Sefat, A.; Nazar, L. F. *Electrochem. Solid-State Lett.* **2003**, *6*, A162.
(5) Gillot, F.; Boyanov, S.; Dupont, L.; Doublet, M.-L.; Morcrette, M.; Monconduit, L.; Tarascon, J.-M. *Chem. Mater.* **2005**, *17*, 6317.
(6) Gillot, F.; Monconduit, L.; Doublet, M.-L. *Chem. Mater.* **2005**, *17*, 5817.
(7) Doublet, M.-L.; Lemoigno, F.; Gillot, F.; Monconduit, L. *Chem. Mater.* **2002**, *14*, 4126.
(8) Gillot, F. ; Bichat, M. P.; Favier, F; Morcrette, M.; Doublet, M.-L.; Monconduit, L. *Electrochim. Acta* **2004**, *49*, 2325.
(9) Bichat, M. P.; Gillot, F.; Monconduit, L.; Favier, F; Morcrette, M; Lemoigno, F.; Doublet, M.-L.; *Chem. Mater.* **2004**, *16*, 1002.
(10) Gillot, F.; Monconduit, L.; Morcrette, M.;Doublet, M.-L.; Tarascon, J.-M.; *Chem. Mater.* **2005**, *17*, 3627.
(11) Gillot, F.; Bernardi, J.; Doublet, M.-L.; Dupont, L.; Monconduit, L.; Morcrette, M.; Tarascon, J.-M. *Chem. Commun.* **2006**, to be submitted.
(12) Poizot, P.; Laruelle, S.; Grugeon, S.; Dupont, L.; Tarascon, J.-M. *Nature* **2000**, *407*, 496.
(13) Grugeon, S.; Laruelle, S.; Dupont, L.; Tarascon, J.-M. *Solid State Sci.* **2003**, *5*, 895.
(14) Badway, F.; Cosandey, F.; Pereira, N.; Amatucci, G. G. *J. Electrochem. Soc.* **2003**, *150*, A1318.

10.1021/cm060433m CCC: $33.50 
Published on Web 06/28/2006

$y$Li$_3$P + M$^0$ conversion reaction. In light of such results, it appears that both the transition metal and the P/M ratio are crucial parameters in the reactivity of these materials toward lithium. To figure out the influence of the P/M ratio, we investigated the electrochemical reactivity of the FeP$_y$ ($y$ = 1, 2, 4) electrodes. The iron monophosphide FeP exhibits much better cycling performances than FeP$_2$ and FeP$_4$. Furthermore, the Li reactivity leads to a direct conversion reaction during the first discharge through a single step, while in the subsequent charge/discharge two distinct processes are clearly identified. We used electrochemical galvanostatic and potentiodynamic measurements, electron microscopy, in situ X-ray diffraction (XRD), and Mössbauer spectroscopy combined with first-principles phase diagram calculations to show that this reversible two-step insertion/conversion process is responsible for the encouraging performances of the FeP electrode. The performances of FeP$_y$ are then discussed as a function of the $y$ ratio.

## 2. Experimental Section

**(a) Synthesis and Characterization.** The orthorhombic FeP (*Pnma*) and FeP$_2$ (*Pmnn*) phases and the monoclinic FeP$_4$ (*P*21/*c*) phase were synthesized at high temperature by placing stoichiometric amounts of iron metal (Fe Alfa Aesar, 350 mesh, 99.9%) and red phosphorus (P Alfa Aesar, 100 mesh, 99%) powders in a sealed evacuated silica ampoule. The samples were heated to 700 °C at a rate of 20 °C/h and held at this temperature for 5 days before being air-quenched. The as-obtained black powders are air-stable. XRD measurements on FeP, FeP$_2$, and FeP$_4$ powders were performed on a Philips X-pert diffractometer using the Co Kα radiation.

**(b) Electrochemical Tests.** Swagelok-type cells were assembled in an argon filled glovebox and cycled using a VMP or a Mac Pile automatic cycling/data recording system (Biologic Co., Claix, France) in a potential window between 2.5−2 and 0.0 V versus Li$^+$/Li$^0$ at a *C*/*n* (1 Li/*n* h) scan rate of $n$ = 5 or 10. These cells comprise a Li metal disk as the negative electrode, a Whatman GF/D borosilicate glass fiber sheet saturated with a 1 M LiPF$_6$ in ethylene carbonate, dimethyl carbonate (DMC; 1:1 by weight) as the electrolyte, and a positive electrode made by mixing the starting transition metal phosphides powder with 15% (weighed) carbon black (SP). Usually, 10−12 mg of the mixed powders is placed on top of the Swagelok plunger. In situ XRD electrochemical cells assembled similarly to our Swagelok cell but with a beryllium window as the current collector on the X-ray side were placed on a Brucker D8 diffractometer (Co Kα = 1.79026 Å), equipped with a PSD detector, and connected to the VMP system. The cell was discharged at a *C*/20 scan rate, and the XRD patterns were dynamically collected for every 0.1 reacted Li, using 5 mV potential steps.

**(c) High-Resolution Transmission Electron Microscopy (HR-TEM).** A Tecnai F20 ST transmission electron microscope (TEM) equipped with energy-dispersive spectrometry (EDS) analysis was used to conduct our TEM/HRTEM investigations. To perform these experiments, the cells were stopped and opened in a drybox once cycled to the required voltage. The discharged or recharged materials were recovered and washed with DMC prior to being placed onto a copper grid mounted on our TEM sample holder. Through a special mobile airlock of our own design, the sample was then transferred to the TEM, without any air exposure, for selected-area electron diffraction (SAED) pattern and bright field image collection.

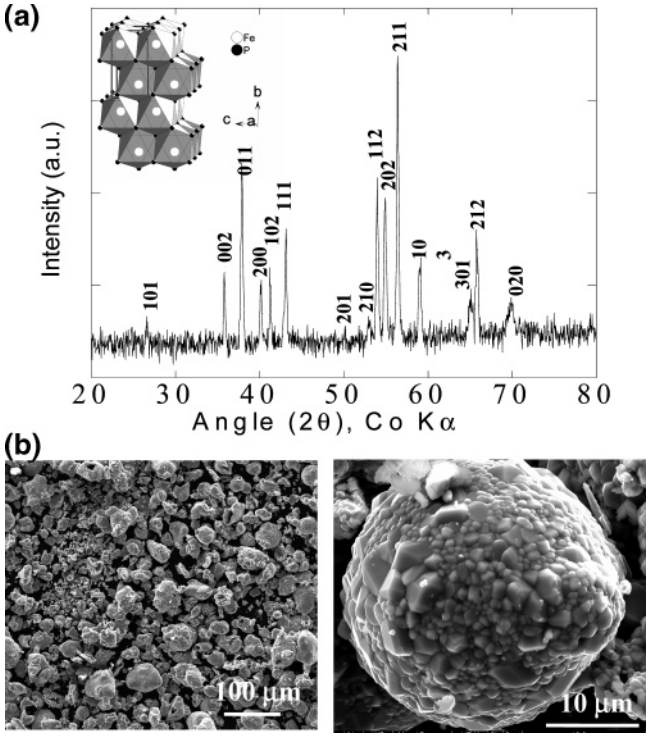


**Figure 1.** (a) XRD patterns (Co Kα) of orthorhombic FeP prepared by a high-temperature ceramic route, with the orthorhombic crystal structure in the inset. (b) SEM images of the FeP powder samples.

**(d) Mössbauer Spectroscopy.** $^{57}$Fe Mössbauer spectra were recorded in transmission geometry in the constant acceleration mode, using equipment supplied by Ortec and Wissel and a $^{57}$Co-(Rh) source of a nominal activity of 10 mCi. The velocity scale was calibrated by means of a room-temperature (RT) spectrum of α-Fe. The hyperfine parameters $\delta$ (isomer shift) and $\Delta E_q$ (quadrupole splitting) were determined by fitting Lorentzian lines to the experimental data, using the ISO program.[15] Isomer shifts are given with respect to the RT spectrum of α-Fe.

**(e) Computational Details.** First-principles density functional calculations were performed in the generalized gradient approximation (GGA) using the PBE functional[16] and the projector augmented waves (PAW) pseudo-potentials,[17] as implemented in the VASP code.[18] Spin polarized calculations were considered to account for the magnetic behavior of Fe nanosized particles and any intermediate phase of the Li−Fe−P phase diagram. The convergence of the calculations was checked with respect to both the energy cutoff (up to 700) and the $k$ points grid (up to 10 × 10 × 10 Monkhorst-Pac mesh) used for the Brillouin zone integration.

## 3. Results

**(a) Synthesis and Characterization.** The XRD pattern of FeP is depicted Figure 1a and reveals sharp Bragg peaks, indicative of a highly crystalline sample, which could all be indexed on the basis of an orthorhombic cell with lattice parameters similar to those reported in the literature ($a$ = 5.193(1) Å, $b$ = 3.099(1) Å, $c$ = 5.792(1) Å, *Pnma*).[19,20] Within the FeP unit cell, Fe is coordinated by six P atoms

(15) Kündig, W. *Nucl. Instrum. Methods* **1969**, *75*, 336.
(16) Perdew, J. P.; Burke, S.; Ernzerhof, M. *Phys. Rev. Lett.* **1996**, *77*, 3865.
(17) Kresse, G.; Joubert, D. *Phys. Rev. B* **1999**, *59*, 1758.
(18) Kresse, G.; Hafner, J. *Phys. Rev. B* **1993**, *47*, 558. Kresse, G.; Furthmuller, J. *Comput. Mater. Sci.* **1996**, *6*, 15.

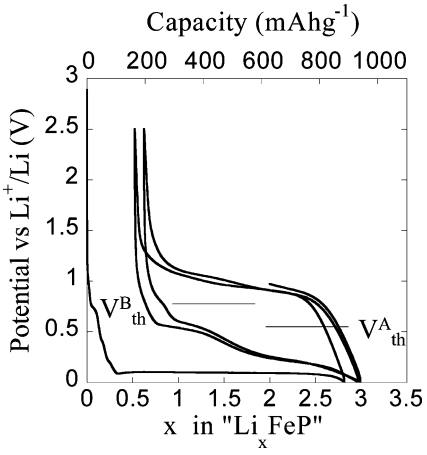


**Figure 2.** Voltage−composition profile of the FeP/Li cell, started in reduction and cycled at a *C*/10 rate between 2.5 and 0 V for the three first cycles. The horizontal solid lines refer to the averaged potentials computed for the insertion ($V_{th}^{B}$) and conversion ($V_{th}^{A}$) reactions.

in a nearly hexagonal configuration with Fe−P distances between 2.186 and 2.447 Å. Some Fe−P distances are smaller than the sum of the covalent radii (1.17 Å) and suggest a high degree of covalence for these bonds, in agreement with previous experimental and theoretical analyses of chemical bonding in transition metal phosphides.[21,22] The structure can be viewed (inset of Figure 1a) as a closely packed $FeP_6$ edge- and face-sharing structure. The powder morphology was investigated by scanning electron microscopy (SEM; Figure 1b) showing 1−5 $\mu$m crystallites intimately nested to form 10−50 $\mu$m grains.

**(b) Electrochemical Properties.** Figure 2 shows the first three cycles of the galvanostatic voltage versus composition curve acquired at a rate of 1 Li/10 h, between 2.5 and 0 V. A flat potential plateau at 0.1 V is observed during the first discharge, associated with a two-phase reaction and with the reactivity of 2.5 Li. Small insertions of 0.1 Li at 0.4 V (process 1) and 0.2 Li at 0.2 V (process 2) are also observed prior to the two-phase reaction, following the expected insertion in carbon black around 0.75 V (process C). Upon charge, 2.3 Li are extracted from the electrode corresponding to a reversible capacity of 720 mA h $g^{-1}$ (4500 mA h $cm^{-3}$). According to the potential derivative curve of Figure 3, two distinct processes occur upon charge and discharge, once the first discharge is achieved. The sharp incremental peak of the first discharge (dotted line) tends to suggest a two-phase conversion reaction $FeP + 3Li \rightarrow Li_3P + Fe^0$, even though the number of exchanged lithium is lower than the expected value. In further cycles, two distinct incremental peaks of capacity are observed, both upon charge (A and B) and upon discharge (B′ and A′). Potentiodynamic experiments carried out with different potential cutoffs clearly demonstrate that processes A (0.92V) and B (1.05 V) upon charge are directly linked to processes A′ (0.21 V) and B′ (0.55 V) upon discharge, respectively (Figure 4). This suggests a good

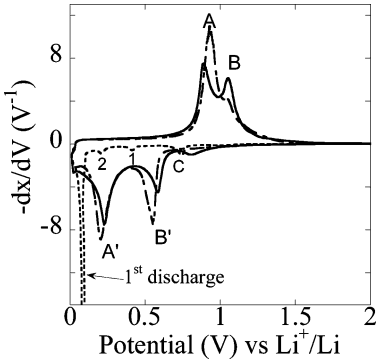


**Figure 3.** Potential derivative −d*x*/d*V* plots of the FeP/Li cell, started in reduction and cycled at a *C*/10 rate between 2.5 and 0 V for the first three cycles. The dotted line corresponds to the first discharge while the dashed and solid lines correspond to the first charge and second discharge and the second charge and third discharge.

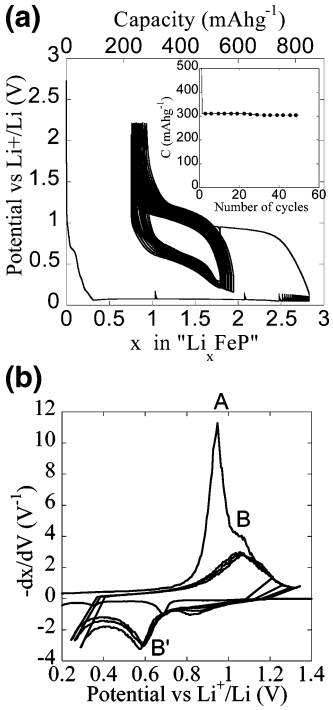


**Figure 4.** (a) Voltage−composition profile and (b) potential derivative −d*x*/d*V* plot obtained for the FeP/Li cell, started in reduction and cycled at a *C*/5 rate between 2.2 and 0.25 V for the 50 first cycles, after a complete first discharge down to 0.05 V. Inset of part a gives the electrode capacity retention for the 50 first cycles.

reversibility of the corresponding reactions, in agreement with a capacity retention of 97% between the second and the third cycles. We note, however, that the relative intensity, the width, and the potential of the incremental peaks evolve along the cycling, suggesting changes in the electrode morphology and, therefore, in the kinetics of the reactions. This may unfortunately be linked to the capacity fading, observed after four cycles. To try to improve the cycling life of the FeP electrode, we checked the relative capacity retention of the two different processes A(A′) and B(B′). As shown Figure 4, only one process occurs upon charge and discharge when the potential window is set to avoid the A′ process. It corresponds to the B(B′) process observed in the full potential window and is associated with the exchange of 1 Li. Interestingly, this process shows a full capacity retention of 310 mA h $g^{-1}$ after 50 cycles (inset in Figure

(19) Nakahara, S.; Chu, S.; Long, J.; Riggs, V.; Johnston, W., Jr. *J. Cryst. Growth* **1985**, *72*, 693.
(20) Fjellvag, H.; Kjekshus, A.; Andersen, A. F. *Acta Chem. Scand., Ser. A* **1986**, *40*, 227.
(21) Grosvenor, A. P.; Wik, S. D.; Cavell, R. G.; Mar, A. *Inorg. Chem.* **2005**, *44*, 8988.
(22) Tong, G. H.; Cheung, A. S. C. *J. Chem. Phys.* **2003**, *118*, 9224.

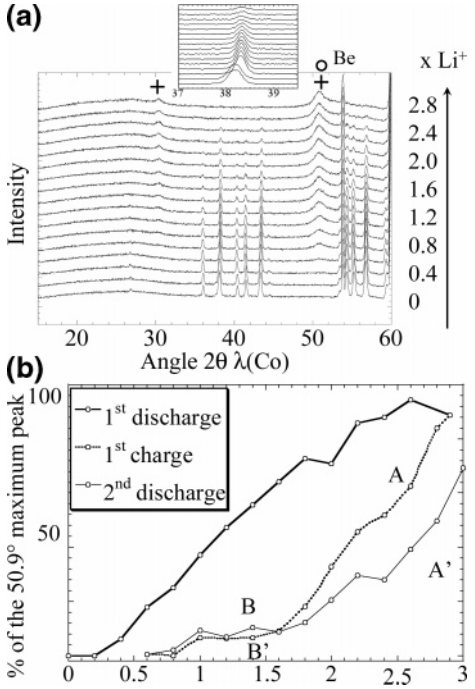


**Figure 5.** (a) In situ XRD patterns dynamically collected for the FeP/Li cell cycled between 2.5 and 0 V at a *C*/20 rate, for the first discharge, using 5 mV potential steps. The Bragg reflections are indicated by stars for the starting phase and by crosses and empty circles for $Li_3P$ and Fe, respectively. An enlarged image of the Bragg diffraction peaks for processes 1 and 2 is given in inset for the discharge. (b) $Li_3P$ surface peak integration of the $Li_3P$ (110)/(103) characteristic peaks for the first and second discharge and the first charge, plotted as a function of *x*.

4a), at a *C*/5 scan rate, suggesting that the capacity fading observed after four cycles in the full potential window is due to a poor reversibility of process A. It should be noticed here that process A(A′) exhibits a much higher polarization (0.7 V) between the charge and the discharge than process B (0.5 V).

**(c) In Situ XRD and HRTEM.** To investigate the structural modifications of FeP upon cycling, in situ XRD patterns were dynamically collected during the first discharge and the first charge for the FeP/Li half cell in the full potential window and for a low *C*/20 scan rate. The two different processes observed in the potential−composition curve of Figure 2 at the very beginning of the discharge (namely, processes 1 and 2), are clearly distinguishable in the XRD patterns. As shown in the inset of Figure 5a, the diffraction peaks of the pristine FeP structure are not affected by the first insertion process (1) while they slightly shift up to higher angles as soon as the second insertion process (2) takes place. This suggests a reaction of 0.1 Li with the electrolyte (1) followed by an insertion of 0.2 Li into the FeP unit cell, associated with slight changes in the FeP cell parameters, from refined $a = 5.188(6)$, $b = 3.116(4)$, and $c = 5.785(9)$ Å to refined $a' = 5.1919(5)$, $b' = 3.1015(3)$, and $c' = 5.7936(6)$ Å. Note that the nonhomogeneous variation of the unit cell parameters (i.e., $\delta a$, $\delta c > 0$, and $\delta b < 0$) has been confirmed by a slight shift down to lower angles and up to higher angles for the ($h0l$) and ($0k0$) diffraction peaks, respectively. After these two first insertion processes, the intensities of the FeP diffraction peaks progressively decrease during the discharge, without showing any significant change in their Bragg angles. Simultaneously,

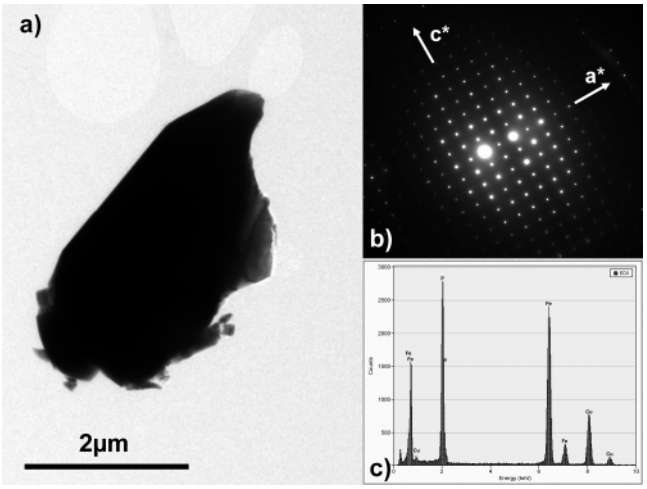


**Figure 6.** (a) Bright field image of the starting FeP material together with (b) the corresponding b* zone axis SAED pattern and (c) the recorded EDS spectrum.

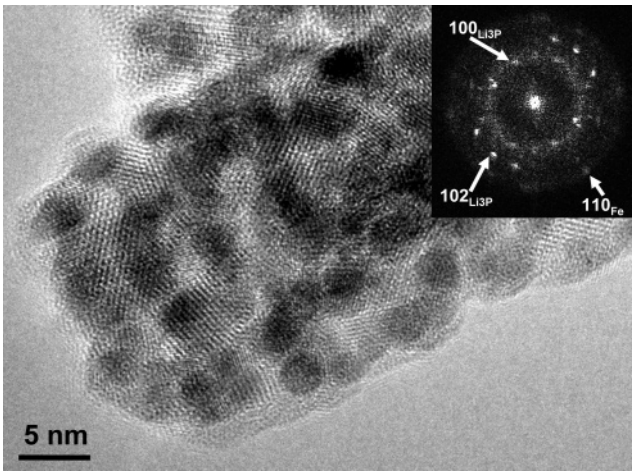


**Figure 7.** HRTEM image realized at the end of the discharge and the corresponding FFT in the inset.

several broad diffraction peaks progressively appear centered at $2\theta = 30.5$ and 50.9°, which can be attributed to the main Bragg reflections of the hexagonal $Li_3P$ phase, indexed with (101) and (110)/(103), respectively. Note that the intensity of the second peak (110)/(103) is larger and broader than expected, suggesting the occurrence of another phase in the electrode. According to the conversion reaction $FeP + 3Li \rightarrow Li_3P + Fe^0$, it is tempting to attribute this contribution to the iron metal, especially because the main diffraction peak of Fe is expected at a very close Bragg angle (52.0°). To confirm this hypothesis, HRTEM measurements were performed on the starting and cycled electrodes. As shown Figure 6a, the initial sample consists of large ceramic particles of several micrometers in size and perfectly crystallized. The SAED pattern of Figure 6b shows them to be pure FeP, as confirmed by the 1:1 Fe/P ratio obtained through an EDS analysis (Figure 6c). When the sample is fully discharged, the initial particles transform into an agglomerate of crystallized 5 nm nanoparticles embedded in a crystallized lithiated matrix, as shown on the HRTEM image of Figure 7. After the calculation of the fast fourier transform (FFT; inset of Figure 7) and indexing of the so-obtained spots, the nanoparticles and matrix are attributed

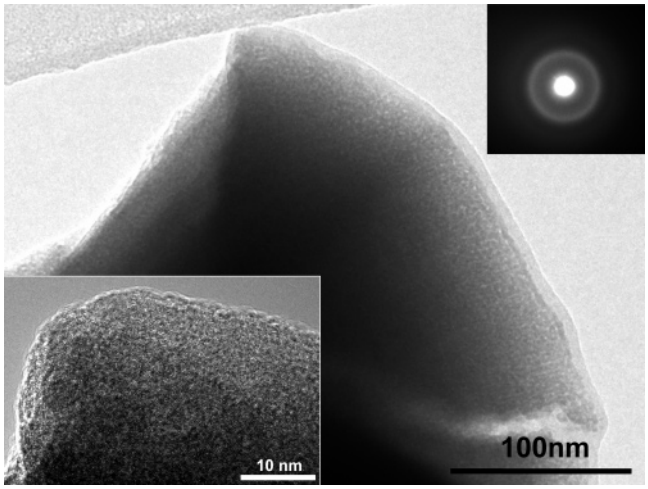


**Figure 8.** Bright field image of a particle of the 3 V recharged electrode. In the insets, the HRTEM image of a part of this particle (bottom) and its corresponding SAED pattern (top).

to metallic iron and $Li_3P$ phases, respectively. The $FeP + 3Li \rightarrow Li_3P + Fe^0$ conversion reaction expected in the first discharge from the large plateau observed in the potential−composition curve of Figure 2 is thus confirmed by in situ XRD and HRTEM analyses. By increasing the discharge rate, we experienced traces of residual FeP, as deduced by X-ray (Supporting Information) indicating that our electrodes suffer from kinetic limitations and leading to incomplete insertion ($x = 2.5$) for higher *C*/10 scan rate (Figure 2).

On charge, the (101) and (110)/(103) characteristic peaks of the $Li_3P$ and Fe phases progressively vanish down to a lithium content close to $x = 1.5$, while no extra peaks appear. This has been confirmed by the HRTEM images recorded on particles at the end of charge and showing no lattice fringe (bottom left inset of Figure 8). This is the signature of an amorphization of the material, often observed on re-charged phosphides and confirmed by the corresponding SAED pattern (top right inset of Figure 8) where one broad ring is observed.

A comparison between the first and second discharges and the first charge leads to interesting results. Figure 5b shows the surface peak integration performed on the (110)/(103) diffraction peak of the $Li_3P$ phase ($2\theta = 50.9°$). While this peak progressively increases during the first discharge, it shows a different evolution on subsequent charge and discharge: it rapidly decreases (respectively increases) upon process A (respectively A′) while it does not evolve upon process B (respectively B′). This shows that $Li_3P$ is involved only in process A(A′), a process which is clearly not fully reversible, as displayed by the intensity decrease observed between the first charge and the second discharge.

## 4. Mechanism

Our results clearly demonstrate that the FeP electrode reacts with Li through a one-step conversion reaction in its first discharge and through a two-step (A + B) reaction in further charges and discharges. Although process B exhibits a better reversibility than process A, the overall capacity retention of the FeP electrode is pretty good compared to that of the $FeP_2$ and $FeP_4$ electrodes (see below). Moreover, the different behaviors observed between the first discharge (one-step reaction) and the subsequent charges and discharges (two-step reaction) have never been reported for any other transition metal phosphides. Unfortunately, as a result of the electrode amorphization upon charge, none of the in situ XRD and HRTEM techniques could help in characterizing the intermediate electrode between process A and process B. Yet, our own experience in binary transition metal phosphides suggests that thermodynamically stable phases with intermediate lithium composition can be obtained by electrochemical processes, with rather low energy costs.[5,6] First-principles electronic structure calculations associated with full structural relaxations can easily seek such reaction paths, by means of reaction enthalpy and phase diagram calculations.

**(a) Phase Diagram Calculations.** Although a proper phase diagram determination requires finite temperature free energy calculations, we believe that entropy contributions will not affect drastically the results and that the main features of the phase diagram should be provided by the $T = 0$ K free electronic energies (i.e., the enthalpies). Following the $FeP + 3Li \rightarrow Li_3P + Fe^0$ conversion reaction demonstrated on first discharge, we computed the $Li_xFeP$ phase diagram from $x = 0$ to $x = 3$, in which the enthalpy associated with every intermediate composition is plotted with respect to the proportional mixture of the FeP and the $Li_3P + Fe^0$ electrodes through the equation

$$Li_xFeP \leftrightarrow (1 - x/3)FeP + x/3(Li_3P + Fe^0) \qquad (1)$$

This way, we get a quasi direct picture of the open circuit voltage, without going through average potential computations. This is particularly useful to avoid taking into account the bulk energy of the Li metal which is known to be badly reproduced by DFT, especially within its local approximation.[23]

Among the possible structures one can envision for the ternary $Li_xFeP$ systems ($0 \leq x \leq 2$) that the P-based face-centered cubic (fcc) network is the most probable model to consider, as deduced from the crystal structure of the $Li_xMP_y$ ternary phases characterized. The P-based fcc unit cell contains eight tetrahedral sites and four octahedral sites. If one assumes the Fe:P ratio to be constant along the complete charge and discharge, four different models can be constructed for the input structures, depending on both the lithium composition and the Li/Fe cationic distributions: (M1) Fe in the four octahedral sites of the fcc unit cell and Li in the tetrahedral sites ($0 \leq x \leq 2$), (M2) Fe and Li in the tetrahedral sites ($0 \leq x \leq 1$), (M3) Fe in half of the tetrahedral sites and Li in the octahedral sites ($0 \leq x \leq 1$), and (M4) Fe in the tetrahedral sites and Li in both the tetrahedral and the octahedral sites ($1 \leq x \leq 2$). Note that each model gives rise to different cationic distributions, for one given lithium composition. These different structures have all been computed, but for sake of clarity, only the most stable phases are considered in the phase diagram. Note that more exotic structures derived from a statistical distribution

(23) Aydinol, M. K.; Kohan, A. F.; Ceder, G.; Cho, K.; Joannopoulos, J. *Phys. Rev. B* **1997**, *56*, 1354.

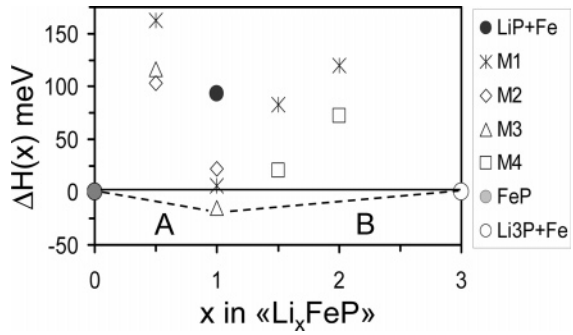


**Figure 9.** First-principles enthalpies $\Delta H(x)$ of the $x$Li/Fe/P systems, computed with respect to the proportional mixture of starting (FeP) and discharged ($Li_3P + Fe^0$) electrodes. The horizontal solid line at 0 meV corresponds to the reference energy of the proportional mixture of FeP and $Li_3P + Fe^0$, and M1, M2, M3, and M4 correspond to the different cubic models used as input structures in the structural relaxation procedure. The dotted lines give the new phase diagram described by two biphasic domains, namely, process A and process B.

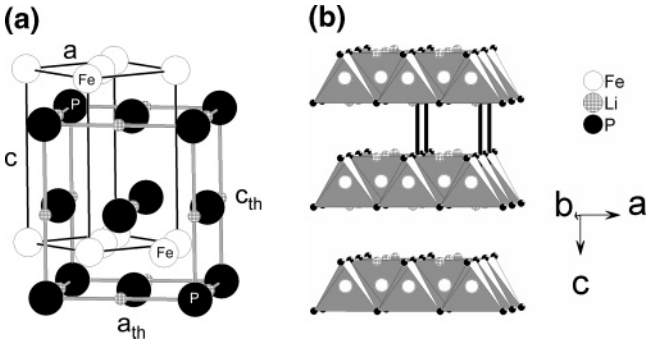


**Figure 10.** (a) Structural relationship between the tetragonal LiFeP unit cell (black box) and the P-based distorted fcc unit cell (grey box) obtained from structural relaxations. Li, Fe, and P are illustrated by hatched, white, and black circles. (b) Crystal structure of the tetragonal LiFeP structure.

of Li and Fe in both the tetrahedral and the octahedral sites were also checked but led to pretty distorted structures associated with much higher energies than those obtained for the more symmetric structures. Another electrode that needs to be considered in the Li−Fe−P phase diagram is the mixed $LiP + Fe^0$ electrode, which is claimed to be achieved on charging the nanocomposite $Li_3P + Co^0$ electrode formed after the complete discharge of the $CoP_3$ electrode.[2]

The results are presented Figure 9, in which the horizontal line corresponds to the reference energy of the conversion reaction $FeP + 3Li \rightarrow Li_3P + Fe^0$. Only one phase turns out to be more stable than this two-phase line. It corresponds to a tetragonal LiFeP phase with $a_{th} = 5.22$ Å and $c_{th} = 5.86$ Å unit cell parameters and was obtained from the structural relaxation of any of the M3-type input structures, in which the Li and the Fe atoms lie in the octahedral sites and in half the tetrahedral sites of the initial fcc lattice, respectively. This result was obtained independently of spin polarizations, suggesting that this ternary LiFeP is not magnetic. Using simple symmetry considerations, one can link this computed structure to the only LiFeP phase ever reported in the literature ($a = 3.6910$ Å, $c = 6.0230$ Å, $P4/nmn$[24]) through the relations $a_{th} = a\sqrt{2}$ and $c_{th} = c$. As shown Figure 10a, such a tetragonal structure (black unit cell box) can be easily

(24) Juza, R.; Langer, R. *Z. Anorg. Allg. Chem.* **1968**, *361*, 58.

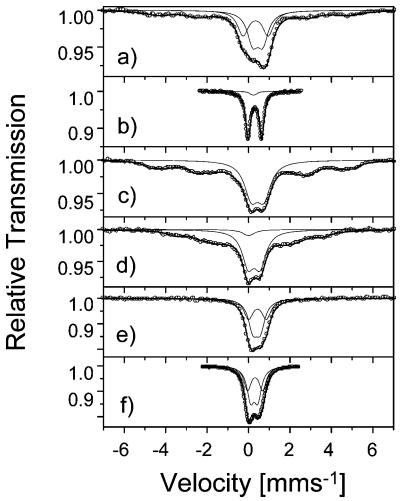


**Figure 11.** $^{57}$Fe Mössbauer spectra obtained from $C/10$ cycled samples for (a, b) the partially discharged electrode at 0.2 V, (c, d) the fully discharged electrode at 0 V, and (e, f) the partially charged electrode at 1 V. In each group, the spectra recorded at both the LNT (top) and the RT (bottom) are presented.

deduced from a distorted fcc unit cell (grey unit cell box) in which the four iron atoms lie on the corners of a basal plane formed by the $z = 1/4$ tetrahedral sites of the initial fcc. The fact that all the $z = 3/4$ tetrahedral sites of the initial fcc are empty is consistent with the tetragonal distortion ($a_{th} = b_{th} \neq c_{th}$) obtained by the first-principles structural relaxation procedure. The LiFeP structure is described by layers of edge-sharing $FeP_4$ regular tetrahedra (Fe−P = 2.344 Å), each layer being surrounded by lithium (Figure 10b). The formation of this phase through electrochemical reaction can be understood by means of P−P bond breaking and easy iron displacements within the starting FeP structure. The driving force of this structural rearrangement should be mainly electronic, as the closely packed crystal structure of FeP prevents any $Li^+$ ionic diffusion into the bulk. Hence, $Li^+$ ions are expected to accumulate at the surface of each crystallite, while the associated electrons fill the strongly delocalized FeP electronic structure to compensate for the cationic charge. This capacitive effect occurring at the crystallite surface has mainly kinetic origin and should decrease by decreasing the scan rate and/or the particle size, in good agreement with the large discrepancy observed between the first and further discharge potentials. The FeP to LiFeP transformation (B′) is expected to occur through a two-phase process, as suggested by the higher enthalpies found for the $Li_xFeP$ phases associated with lithium contents smaller than $x = 1$ (Figure 9). Note that the formation of the nanocomposite $LiP + Fe^0$ electrode is here shown to be disfavored by not less than 100 meV per unit cell.

**(b) Mössbauer Spectroscopy.** To corroborate this mechanism, we used $^{57}$Fe Mössbauer spectroscopy to characterize the electrode during the first discharge (0.2 V), at the very end of the first discharge (0 V), and during the first charge (1 V), that is, after the full completion of process A. Spectra were recorded at both liquid nitrogen temperature (LNT) and RT. Figure 11a shows the $^{57}$Fe Mössbauer LNT spectrum recorded at 0.2 V. It consists of two doublets and a sextet, the latter with strongly broadened lines, indicating the presence of a magnetically ordered phase with a broad

distribution of hyperfine magnetic field strengths on the iron sites. The appearance of a magnetic phase is expected from the reaction mechanism proposed for the first discharge $FeP + 3Li \rightarrow Li_3P + Fe^0$. We thus attribute this sextet to small particles of α-Fe with a high fraction of surface atoms having a reduced number of magnetic neighbors and experiencing lower local field strength than in bulk α-Fe. HRTEM shows that the size of these particles reaches 5 nm at the end of the discharge. The particles of this Mössbauer sample at 0.2 V can thus be expected to be smaller than 5 nm, as previous works on nanosized α-Fe[25−27] show that particles up to 5 nm in size reveal super-paramagnetic behavior in RT Mössbauer spectra. The RT spectrum of the present sample, given in Figure 11b, shows only the characteristic doublet of FeP, with hyperfine parameters ($\delta = 0.31$ mm/s and $\Delta E_q = 0.66$ mm/s) in good agreement with literature,[28] but not the singlet at $\delta = 0$ expected for the super-paramagnetic α-Fe. Instead we see a further doublet with $\delta = 0.24$ mm/s and $\Delta E_q = 0.16$ mm/s. Apparently, the metallic particles are so small that no metallic core is formed and all atoms are in contact with a surrounding FeP or $Li_3P$ matrix, leading to nonzero hyperfine parameters $\delta$ and $\Delta E_q$. The LNT spectrum obtained at the end of the discharge (Figure 11c) shows residual FeP and the sextet of the metallic phase, with an increased spectral weight of the latter, as compared to the partially discharged sample, indicating further transformation of FeP into $Li_3P + Fe^0$. The residual FeP occurring at the end of discharge is consistent with the *C*/10 scan rate (same as for Figure 2) used for this experiment. Moreover, the distribution of the local magnetic fields extends to higher values than before, which we attribute to an increased particle size. The RT spectrum (Figure 11d) still shows the doublet of residual FeP and a magnetically split component deformed by dynamic effects. The shape of the central part of the spectrum suggests the presence of a singlet at $\delta = 0$ mm/s from super-paramagnetic iron, in agreement with previous observations made for 5 nm particles of α-Fe.[26] No magnetic phase is seen in the LNT spectrum obtained for the partially charged sample (Figure 11e), in agreement with the proposed transformation of $Fe^0$ to LiFeP. The RT spectrum (Figure 11f) reveals the presence of two phases. The hyperfine parameters of the first ($\delta = 0.32$ mm/s, $\Delta E_q = 0.73$ mm/s) are close to that of FeP. We thus associate this doublet with the residual FeP phase characterized in the XRD patterns all along the first cycle. The second doublet is characterized by a lower quadrupole splitting as compared to FeP ($\Delta E_q = 0.38$ mm/s), indicating a local environment around iron of higher symmetry than in FeP, where iron is found in a distorted hexagonal configuration with Fe−P distances between 2.186 and 2.447 Å. It could correspond to the local environment in LiFeP, which is highly symmetric with iron surrounded by four phosphorus atoms at equal distances of 2.344 Å. Although the hyperfine parameters of LiFeP have not yet been reported, we associate this doublet with LiFeP.

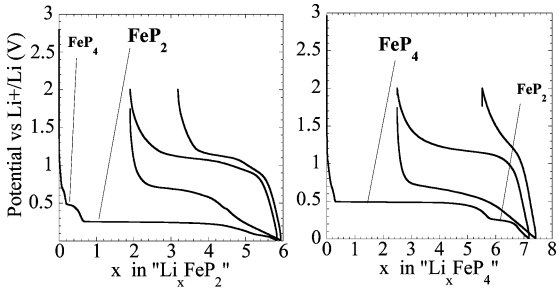


**Figure 12.** Potential−composition profiles for (a) the $FeP_2$/Li and (b) the $FeP_4$/Li cells, started in reduction and cycled between 2 and 0 V, at a scan rate *C*/5.

The combination of Mössbauer spectroscopy and phase diagram computations thus shows that a tetragonal LiFeP phase can be formed through redox chemistry starting from either the FeP electrode (reduction) or the $Li_3P$+$Fe^0$ electrode (oxidation). The two reversible reactions expected for processes A and B should therefore correspond to

$$(B' \leftrightarrow B) \quad FeP + Li \leftrightarrow LiFeP \tag{2}$$

$$(A' \leftrightarrow A) \quad LiFeP + 2Li \leftrightarrow Li_3P + Fe^0 \tag{3}$$

As a result of the large particle sizes of the pristine FeP material that gives rise to weak $Li^+$ diffusion and, therefore, kinetic limitations, the $FeP + Li \rightarrow LiFeP$ two-phase reaction should be blocked on the first discharge, leading to the direct $FeP + 3Li \rightarrow Li_3P + Fe$ conversion reaction. From a thermodynamic point of view, the formation of LiFeP is expected to be favored ($\Delta H = -0.77$ eV/Li) compared to the direct conversion ($\Delta H = -0.63$ eV/Li). The pretty good agreement obtained between the experimental and the computed potentials for processes A (A′) and B (B′) and displayed Figure 2 ($V_{th}^A$ and $V_{th}^B$), together with the pretty bad agreement obtained between the experimental ($V_{exp} = 0.10$ V) and the computed ($V_{th} = 0.63$ V) potentials for the direct conversion reaction, gives rather clear evidence of much larger kinetic effects in first discharge than in further cycles, as previously discussed. Note that prior to the conversion reaction of the first discharge, a small amount of lithium is expected to insert into the large agglomerates of microstructured FeP crystallites, thus favoring an efficient electrode grinding.

At this stage, a comparison between the different $FeP_y$ ($y = 1, 2, 4$) electrodes is interesting. As shown Figure 12, the $FeP_2$ and $FeP_4$ electrodes exhibit very close behaviors in their first discharge compared to FeP. The large incremental peaks observed in Figure 13 for the two electrodes can unambiguously be attributed to direct conversions of $FeP_y$ into $yLi_3P + Fe^0$, occurring at 0.25 V and 0.50 V for $y = 2$ and 4, respectively. Nevertheless, both electrodes show much lower capacity retentions than FeP. At first glance, this capacity loss could be related to the occurrence of impurities, as $FeP_2$ and $FeP_4$ starting materials are contaminated by FeP

(25) Tartaj, P.; Gonzales-Carreno, T.; Bomati-Miguel, O.; Serna, C. J.; Bonville, P. *Phys. Rev. B* **2004**, *69*, 94401.
(26) Bødker, F.; Mørup, S.; Pedersen, M. S.; Svedlindh, P.; Jonsson, G. T.; Garcia-Palacios, J. L.; Lazaro, F. J. *J. Magn. Magn. Mater.* **1998**, *177−181*, 925.
(27) Bødker, F.; Mørup, S.; Linderoth, S. *J. Magn. Magn. Mater.* **1995**, *140−144*, 373.
(28) Bailey, R. E.; Duncan, J. F. *Inorg. Chem.* **1967**, *6*, 1444.

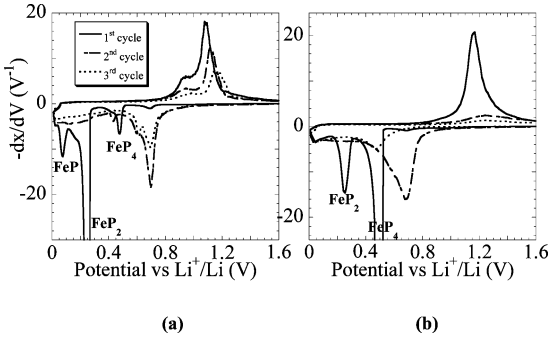


**Figure 13.** Potential derivative $-dx/dV$ curves for (a) the $FeP_2$/Li and (b) the $FeP_4$/Li cells, started in reduction and cycled between 2 and 0 V, at a scan rate *C*/5.

and $FeP_4$ and by $FeP_2$, respectively. The weight ratio of these $FeP_y$ impurities is, however, weak regarding their related incremental peaks in the potential derivative curves of Figure 13, in the first discharge. Moreover, whatever the impurity ratio, the achievement of these $MP_y$ conversion reactions leads to chemically equivalent discharged electrodes, all made of $Fe^0$ nanoparticles embedded in a $Li_3P$ matrix. The discharged electrodes should, therefore, differ from an electrochemical point of view, as the occurrence of an increasing amount of $Li_3P$ obviously alters their redox behavior. As we showed for FeP, an intermediate LiFeP phase is formed upon charge from the $Li_3P + Fe^0$ electrode, through process A, occurring around 0.92 V. Interestingly, a process occurs at the same potential for the $FeP_2$ electrode, while nothing is observed for the $FeP_4$ electrode at this potential. We believe that this process cannot be solely attributed to the FeP impurity in $FeP_2$, because (i) the FeP/$FeP_2$ weight ratio is given to be less than 10% by XRD and (ii) the large incremental peak following this first process upon charge occurs at the same potential (1.08 V for $FeP_2$ vs 1.05 V for FeP) as the LiFeP $\rightarrow$ FeP + Li transformation (process B) suggested for the FeP electrode. This suggests a *y*-independent mechanism upon charge for the two FeP and $FeP_2$ electrodes, that is, the formation of LiFeP in both cases. Such a hypothesis is reasonable because no thermodynamically stable $Li_xFeP_2$ phase could be found, either in the computed $FeP_2$ phase diagram or in the literature. It would imply an intermediate LiFeP + $Li_3P$ electrode upon charge from the $2Li_3P + Fe^0$ electrode and upon discharge from a hypothetic "FeP + $Li_3P$" in the case of $FeP_2$. The poorer reversibility of A (A′) and B (B′) in $FeP_2$ compared to FeP could thus originate from kinetic factors, as a less efficient diffusion of the $Fe^0$ nanoparticles is expected into the $yLi_3P$ matrix, when *y* increases. For $FeP_4$, only one incremental peak is observed upon charge at 1.16 V, suggesting another mechanism, preventing the intermediate LiFeP electrode. The larger polarization observed for this electrode is consistent with its very poor reversibility and supports the impact of the $y = P/M$ ratio on the reconstruction of either LiFeP + $yLi_3P$ or $MP_y$. Additional experimental and computational studies are here needed, especially to improve the purity of the starting $FeP_2$ and $FeP_4$ electrodes and to elucidate the mechanism of the $FeP_4$ electrode.

## Conclusion

The reactivity of $FeP_y$ electrodes toward lithium have been investigated through combined experiments and first-principles calculations. Direct conversion reactions are clearly demonstrated for all starting $FeP_y$ ($y = 1, 2, 4$) on first discharge, leading to composite electrodes described by nanosized $Fe^0$ particles embedded into $yLi_3P$ matrixes. The first-principles $Li_xFeP$ phase diagram computations reveal that a thermodynamically stable LiFeP intermediate phase is achievable through electrochemical process, either in oxidation from the $Li_3P + Fe^0$ electrode or in reduction from the FeP electrode. This means a two-step insertion/conversion reaction (FeP + Li $\rightarrow$ LiFeP and LiFeP + 2Li $\rightarrow$ $Li_3P + Fe^0$) for the FeP electrode, after the one-step conversion reaction (FeP +3Li $\rightarrow$ $Li_3P + Fe^0$) in the first discharge. This result is corroborated by (i) the potentiodynamic curves displaying two well distinct A (A′) and B (B′) processes upon charges and discharges associated with a better capacity retention for the B(B′) process, that is, LiFeP $\leftrightarrow$ FeP + Li, (ii) the in situ XRD showing a nucleation delay of $Li_3P$ in the second discharge compared to the first discharge, (iii) the Mössbauer spectroscopy analysis ruling out both the occurrence of $Fe^0$ nanoparticles during the insertion process and the formation of a $LiP + Fe^0$ electrode already suggested for another transition metal phosphide ($CoP_3$), and (iv) first-principles calculations leading to well-reproduced averaged potentials for processes A (A′) ($V_{th}^A = 0.55$ V) and B (B′) ($V_{th}^B = 0.77$ V). We believe the low potentials observed in the first discharge for the $FeP_y$ direct conversion ($V_{exp} = 0.10$, 0.25, 0.50 V for $y = 1, 2, 4$, respectively) are mostly linked to kinetics, as displayed by the poor agreement obtained with the computed (thermodynamic) potentials ($V_{th} = 0.63$, 0.79, 0.91 V for $y = 1, 2, 4$, respectively). Capacitive effects linked to the accumulation of $Li^+$ at the electrode grain surfaces should be responsible for the first discharge low potential, owing to drastic morphological changes between the pristine material (highly crystallized) and the fully recharged "FeP". Work is in progress to minimize the discrepancy in the first and further discharge potentials, by decreasing the scan rate.

**Acknowledgment.** The computational part of this work was supported by the French computational resources centers IDRIS and CINES (Project No. lsd2402) under Contract N*o*. 051750. M.-L.D. and J.B. would like to thank the ADEME (Agence de l'Environnement et de la Maîtrise de l'Energie) for its financial support through a Ph.D. grant.

**Supporting Information Available:** In situ XRD patterns dynamically collected for the FeP/Li-metal cell between 2.5 and 0 V at a *C*/10 scan rate using 5 mV potential steps are provided, for both the first discharge and the first charge (JPEG). The Bragg reflections are indicated by stars for the starting FeP phase and by crosses and empty circles for $Li_3P$ and Fe, respectively. This material is available free of charge via the Internet at http://pubs.acs.org.

CM060433M